

Radiative cooling instability in 1D colliding flows

Rolf Walder¹ and Doris Folini^{1,2}

¹ Institut für Astronomie, ETH-Zentrum, CH-8092 Zürich, Switzerland;

E-mail: walder@astro.phys.ethz.ch,

² Seminar für Angewandte Mathematik, ETH-Zentrum, CH-8092 Zürich, Switzerland;

E-mail: folini@astro.phys.ethz.ch

Received ... ; accepted ...

Abstract. Radiative shock waves show a strong cooling instability at temperatures above approximately $2 \cdot 10^5$ K. We numerically investigate this instability by simulating different astronomical objects in which colliding flows play an outstanding role: Wind bubbles, supernova remnants, and colliding winds. Computing the flow of each object over a large part of its evolutionary time and resolving all physically relevant scales, we find several phenomenologically different types of this instability. If two smooth flows collide, the instability follows a periodic limit cycle with two modes being important. The connection between the radiative loss function and the mode and type of the over-stability is discussed. The collision of non-smooth flows can temporarily result in an aperiodic evolution of the system. After a characteristic relaxation time the instability then becomes periodic again. Such disturbances as well as violent types of the instability can excite oscillations of the thin layer of cold compressed gas downstream of the shock, which in turn can influence the stability of the radiative shock.

Key words: Hydrodynamics – Instabilities – Shock waves – ISM:kinematics and dynamics – Numerical methods

substantially ionize and heat the matter. As the heated matter cools, it is compressed into thin dense layers. The radiative cooling itself and the presence of a dense layer of cooled gas greatly influence the emitted spectrum. Radiative cooling of shock heated matter leads to emission mostly in the frequency range between X-ray and UV. The cold layer emits mostly in the radio, IR, optical, and UV. Therefore, a better understanding of radiative shock waves, therefore, is crucial for the interpretation of the observed spectra.

Of similar significance is the influence of radiative shock waves on the dynamical shaping of their environment. The cold layer is much denser than the surrounding matter and often prey to instabilities of various types. In addition, the neighboring shock heated zones are often subject to thermal instabilities. Such effects can be crucial for the distribution and the state of the matter in the vicinity of radiative shocks.

In this paper, we study the thermal instability of radiative shock waves in the context of colliding flows. Radiative cooling is included as $\epsilon = N^2 \Lambda(T)$, where $\Lambda(T)$ is piecewise linear on a log-log scale. The necessary spatial resolution to resolve all the relevant length and time scales is provided by an adaptive mesh refinement algorithm. In contrast to previous investigations, we follow the long term evolution of the entire interaction zone. In the case of a decelerating interaction zone this leads to an automatic scanning of wide ranges of the steady state shock velocity. This enables us to make a systematic study of the cooling instability. It also allows us to investigate the mutual influence of the cooling layer and the cold dense layer. In agreement with other authors, we find that for smooth flows the system is overstable: the instability is oscillatory and two different modes are important. The phenomenology of the over-stability, however, may be very different within one mode which leads us to the introduction of phenomenological types. In the case of density disturbances upstream of the interaction zone, a temporarily aperiodic evolution can result for which we give constraints. Finally,

1. Introduction

1.1. Radiative shocks

Shock waves become radiative if the dynamical time of the flow exceeds the cooling time of the shocked matter. Radiative shocks are present in a variety of astrophysical objects: e.g. in supernova remnants, in colliding winds of binary star systems, in accretion processes, in all wind driven structures, in young stellar objects, in galactic and extragalactic jets, in star burst galaxies, in active galactic nuclei. Usually, such shocks are sufficiently strong to

Send offprint requests to: R. Walder

we emphasize the importance of the cold dense layer for the thermal instability of the cooling layer.

1.2. The thermal cooling instability

Catastrophic cooling and the overstability of radiative shock waves due to thermal instability of radiative cooling have been known for several decades. First numerical investigations of catastrophic cooling in shock heated plasmas were carried out by Falle (1975,1981). First numerical investigations of the overstability of radiative shock waves were made by Langer et al. (1981,1982) for the case of accretion flows onto compact objects.

Chevalier & Imamura (1982) (CI in the following) performed a linear stability analysis for a planar flow against a wall as a model for accretion flows. They applied a cooling law of the form $\dot{\epsilon} = N^2 \cdot T^\beta$, and found the cooling layer between the accretion shock and the wall to be thermally unstable for $\beta < \beta_c$. An infinite number of modes with successively higher eigenfrequencies were found, among them a fundamental and a first overtone mode, for which $\beta_c \lesssim 0.4$ and 0.8 respectively. Numerical simulations carried out by Imamura et al. (1984) were in agreement with these results. Wolff et al. (1989) and Imamura & Wolff (1990) extended these investigations to two-temperature models with heat conduction and different cooling processes such as Compton cooling and relativistic Bremsstrahlung. They still found the same modes of the overstable oscillation of the radiative accretion shock.

In a beautiful analytical paper, Bertschinger (1986) extended the analysis to interstellar shocks. He showed that under certain conditions there exists a piecewise self-similar solution in spherical symmetry. The flow pattern is more complex than for accretion flows: a leading shock, a cooling layer behind the shock, a hot or cold interior, and a thin layer of already cooled, compressed gas between the interior and the cooling layer. Performing a linear stability analysis on this solution that allowed for disturbances in all three spatial directions, he found two types of instabilities, a thermal and a dynamical one. For the thermal one he found the same unstable modes in the radial direction as Chevalier & Imamura (1982). Surprisingly, he found that no new modes are introduced by nonradial disturbances. But modes stable to radial perturbations can be unstable to nonradial perturbations.

On the numerical side, significant progress has been made by including detailed radiation processes into the analysis. Innes et al. (1987) (IGF in the following) and Gaetz et al. (1988) (GEC in the following) considered ionization and recombination processes as well as time-dependent non-equilibrium cooling. They agreed on the onset of the instability for shocks having velocities above 130 km/s – 150 km/s. GEC found this instability to be oscillatory which is in agreement with further investigations presented by Innes (1988).

Recently, Plewa (1995) studied strong shock waves ($v_S > 1000$ km/s) running into dense material and found overstable behavior also under these conditions.

In spherical symmetry, stability analyses of radiative shocks were performed by Imamura & Wolff (1990), Houck & Chevalier (1992), and Dgani et al. (1995). Spherically symmetric cooling shells have significantly different stability properties as long as their size is comparable to the relevant radius. For small cooling shells, the stability behavior approaches the planar limit behavior. Attempts to analyze the thermal cooling instability of two-dimensional planar shocks have been made by Strickland & Blondin (1995).

The organization of the article is as follows: In Sect. 2 we briefly describe our physical model. In Sect. 3, this is followed by some notes on the applied numerical methods. In Sect. 4 the basic flow patterns are described and the sample of computations is presented. The thermal cooling instability for the case of smooth flows is analyzed in Sect. 5, and in Sect. 6 the same is done for the case of disturbed flows. The evolution of the cold dense layer is investigated in Sect. 7. In Sect. 8 we discuss our results, and, finally, we present the conclusions in Sect. 9.

2. The physical model

2.1. The governing equations

Our physical model is based on the Euler equations and the use of parameterized radiative loss functions (RLFs in the following). We numerically solve the Euler equations in spherical symmetry:

$$\frac{\partial \rho}{\partial t} + \frac{\partial \rho v_r}{\partial r} = -\frac{2v_r}{r} \rho, \quad (1)$$

$$\frac{\partial (\rho v_r)}{\partial t} + \frac{\partial (\rho v_r^2 + p)}{\partial r} = -\frac{2v_r}{r} \rho v_r, \quad (2)$$

$$\frac{\partial E}{\partial t} + \frac{\partial [v_r (E + p)]}{\partial r} = -\frac{2v_r}{r} (E + p) - \dot{\epsilon}(T, N) + q(T). \quad (3)$$

Here, ρ denotes the mass density, v_r the radial velocity, p the pressure, $\dot{\epsilon}(T, N)$ the cooling term, and $q(T)$ the heating term. The last two are discussed below. The total energy density E is the sum of the thermal energy density U and the kinetic energy density:

$$E = U + \rho v_r^2 / 2. \quad (4)$$

ρ and the number density N are connected by

$$\rho = N \mu m_H, \quad (5)$$

where m_H denotes the mass of the hydrogen atom and μ the mean atomic weight. In our calculations we always use $\mu = 1.3$.

This set is closed by a polytropic equation of state (with $\gamma = 5/3$ in all our calculations),

$$U = \frac{p}{\gamma - 1}. \quad (6)$$

The temperature is given by the ideal gas law as

$$T = \frac{p\mu m_H}{\rho k_B}. \quad (7)$$

This model excludes heat conduction which is probably important for strongly shocked astrophysical plasmas.

2.2. The cooling model

We describe the radiated energy density per time, $\dot{\epsilon}$, by a temperature dependent RLF $\Lambda(T)$ times the number density squared,

$$\dot{\epsilon}(T, N) = N^2 \cdot \Lambda(T). \quad (8)$$

For the RLF $\Lambda(T)$ we use the approximation

$$\Lambda(T) = \Lambda_{0_i}(T)T^{\beta_i}, \quad T \in [T_i, T_{i+1}]. \quad (9)$$

RLFs have been published by several authors. The functions vary significantly depending on the different physical processes which are included. The assumed elemental abundances are of great importance for the RLF. The first radiative loss function (RLF1) we used is a fit to an optically thin, time independent RLF taken from Cook et al. (1989) which uses solar photospheric abundances. The second loss function (RLF2) is a fit to an optically thin, time dependent radiative loss function taken from Schmutzler & Tscharnuter (1993) which uses Allen's abundances. This RLF has been obtained by a thermally self-consistent, time-dependent computation of the cooling of a plasma from 10^9 K to 10^2 K. Both RLFs are shown in Fig. 1 and their exact values are given in Tables 2 and 3 in the appendix. In all our calculations $\dot{\epsilon}$ is set to zero for temperatures below a threshold temperature T_C .

Our cooling model neglects processes which cool only linearly in the density, e.g. cooling by inverse Compton scattering. The use of RLFs also completely neglects ionization and recombination processes. Therefore, we probably overestimate the post-shock temperature as the kinetic energy converted by the shock is only used to heat the matter. Moreover, in reality, the newly shocked matter is likely to be underionized whereas gas on its cooling track tends to be overionized. Consequently, the gas may radiate at a considerably different rate from the equilibrium value used for RLF1. It probably also radiates at a considerably different rate than computed by the time-dependent RLF2, since the two cooling histories and thus the ionization structures do not correspond. The consequences of these simplifications are discussed in Sect. 8.

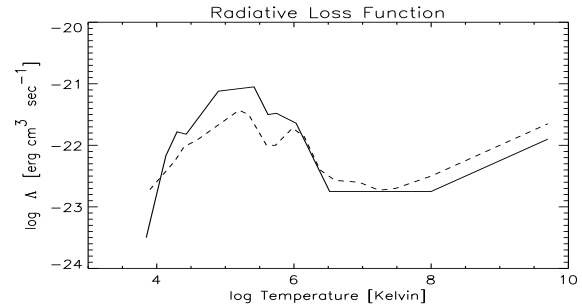


Fig. 1. The two RLFs used: Cook et al. (1989) (solid line) and Schmutzler and Tscharnuter (1993) (dashed line).

Therefore, our physical model is more approximate than the models of IGF and GEC. However, the use of an RLF has the big advantage to be simple enough to allow an analysis of the connection between the RLF and the response of the system. At the same time, it exhibits already most of the features which are characteristic for radiative cooling processes behind shocks. Moreover, the computational costs are sufficiently low to allow a systematic study.

For later use we give the expression for the cooling time τ (by use of eqs. 8, 9 and $U = 3/2kT$),

$$\tau(T, N) = \frac{T}{|dT/dt|} = \frac{3k}{2\Lambda_{0_i}} \frac{T^{1-\beta_i}}{N}. \quad (10)$$

2.3. The heating model

To account for radiative heating of the flow we have introduced a heating term which, for temperatures below a certain threshold temperature $T_H \leq T_C$, sets the gas temperature to T_H .

3. The numerical methods

3.1. The AMRCART code

Equations 1–4 and 6 are solved by the spherically symmetric version of our AMRCART code¹ on the basis of a Cartesian discretization. AMRCART combines a modern high resolution Eulerian MUSCL scheme developed by Colella & Glaz (1984) with the adaptive mesh refinement algorithm by Berger (1985). It automatically refines the spatial grid and the time-step when the local truncation error is estimated to be bigger than a given threshold. This code was originally designed by Berger & LeVeque (1989) for pure gas-dynamics in two space dimensions. It was adapted by Walder (1993) to compute complex astrophysical problems, including reactive flows and arbitrary physical source terms in one, two, and three space dimensions.

¹ A public version of the code will soon be available. Requests please to walder@astro.phys.ethz.ch.

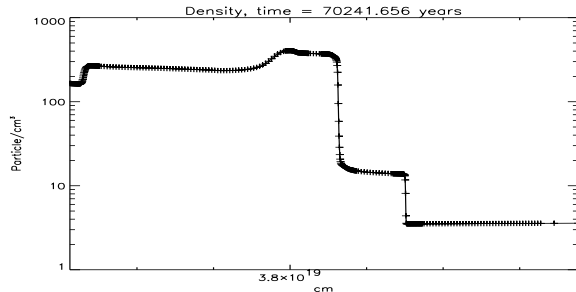


Fig. 2. Illustration of the mesh refinement algorithm. Shown are a computed density profile and the numerical mesh. Three levels (out of five) of refinement are shown. The mesh size is automatically refined by the code.

The mesh refinement algorithm is crucial to the quality of our simulations. Fig. 2 shows how finer meshes are created to improve the spatial resolution where it is needed. In regions with refined meshes the time-step is reduced by the same factor as well. Thus, each time-scale which is dynamically important can be resolved numerically. We emphasize that even in regions with extreme high densities, and at temperatures at which the RLF $\Lambda(T)$ is at its maximum, the radiative energy loss of each cell during one time step Δt is at most one percent of the current thermal energy in this cell in all our calculations.

3.2. Some technical details

In all presented results the center of symmetry is located outside the left boundary of the computational domain. At the left boundary we use reflecting (supernova remnant) or inflow boundary conditions (wind bubble and colliding winds). We use free outflow conditions at the right boundary.

3.3. A note on the numerical error

Numerically obtained solutions are approximate solutions. Therefore, one should always convince oneself that the numerical solution is sufficiently close to the correct one. Figure 3 shows the significant, even qualitative difference between a *high*- and a *low-resolution* numerical solution of an unstable wind bubble (model WB1 of Table 4). They have been calculated with a finest spatial discretization of about $2.4 \cdot 10^{13}$ cm and $1.92 \cdot 10^{14}$ cm respectively. The size of the computational domain is 10^{20} cm. In both calculations the cfl-number has been fixed to 0.2. Thus, the time-steps differ by a factor of 8 as well. Note that even the low-resolution calculation has still a remarkably good resolution compared to most computations given in the literature.

This large error can be pinned down to the numerical smearing of the boundary interface between the cooling layer and the cold compressed layer. In connection

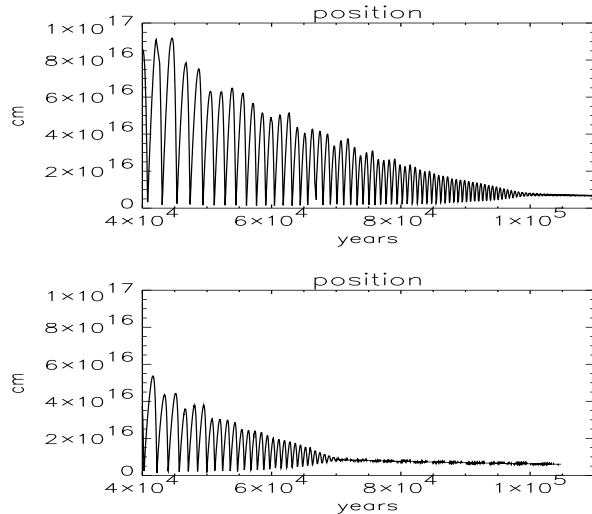


Fig. 3. High- (top) and low-resolution (bottom) simulation of the wind bubble model WB1. Shown is the computed size of the radiative shock. The high-resolution simulation shows a bigger oscillation amplitude and the oscillation lasts nearly twice as long as in the low-resolution simulation. Note that in the high-resolution case the oscillation continues after $110'000$ years but is substantially smaller after having undergone a mode-transition (see Fig. 7).

with stiff source terms (radiative cooling in our case), a too broad smearing of the interfaces can cause unphysical wave speeds (see e.g. LeVeque & Yee 1990, Colella et al. 1986 or Klingenstein 1994). This problem is inherent to each numerical algorithm which is based on interface capturing by finite volumes.

We estimate the errors of our calculated interface speeds to be at most a few percent.

4. Investigated flows

Simulations of wind bubbles (WB), supernova remnants (SNR) and colliding winds (CW) are the basis for our study. These flows are well documented in the literature and we give here only the characteristics needed for this work. A WB (see Fig. 4) is the structure which results when a strong stellar wind blows into the uniform interstellar medium. Similarly, a SNR is the result of a strong explosion driving expelled gas against the uniform interstellar medium. In the case of CW, a fast wind sweeps up a slower predecessor wind from the same star. In the *adiabatic case*, all three flows are self-similar. The leading shock decelerates in the WB-case according to $v_s \propto t^{-2/5}$ (v_s denotes the shock velocity, t the time) and in the SNR-case according to $v_s \propto t^{-3/5}$. Ryu & Vishniac (1991) give a nice overview of these flows. In the CW-case, the velocity of the leading shock is constant (Chevalier & Ima-mura 1983). If *cooling is included* the flows are no longer self-similar. However, Bertschinger (1986) shows that un-

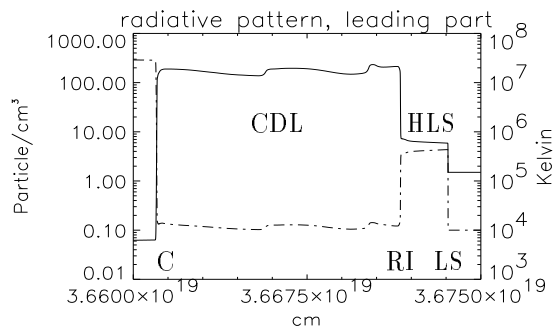


Fig. 4. Leading part of the interaction zone in the radiative case. For details see text.

der certain conditions radiative SNR and WB can be described by piecewise self-similar solutions.

We are interested in flows where the cooling layer is small against the radius of the structure. In this case – despite their different driving mechanisms – WB, SNR and CW have a similar leading part of the interaction zone where the two flows collide. The leading part of the interaction zone is illustrated in Fig. 4 at the example of the WB. In all three cases, it consists of a leading shock (LS), a hot leading shell in which the shocked material cools (HLS) and a ‘cold’ dense layer with compressed, already cooled shocked material (CDL). The HLS is subject to the cooling instability, the CDL can play an important role for the evolution of this instability. We are interested in these two parts. The contact discontinuity (C) marks the rear end of the leading part of the interaction zone. Notice that in our study the reverse shock is nearly adiabatic since – due to the much lower density and the much higher temperature – the cooling time is considerably longer than the dynamical time. In the following we do not discuss this reverse, driving part of the flow.

We list the exact settings of all our calculations in Table 2 in the appendix. We performed SNR and WB simulations with different parameters up to the time where the thermal instability ceased (see Fig. 3). CW were performed over a dynamical time which is equal to approximately 600 cooling times of the leading shell. All three flows have been calculated with both RLFs given in Sect. 2.2 and in the appendix. The results presented below are the quintessence of all these calculations. Of major importance is the WB calculation. Since the structure moderately decelerates, it is possible to scan a wide range of post-shock temperatures (in our case from $T \approx 10^{6.5}$ K to $T \approx 10^5$ K) while the global conditions remain nearly constant over one oscillation period of the instability.

5. The cooling instability of the leading shell for colliding smooth flows

In this section we present the results for the case where two smooth flows collide. In Sect. 6 we investigate the instability for disturbed flows. At present, smoothness means

that during one oscillation cycle the conditions for the radiative shock remain nearly constant. In Sect. 6 we give more thorough constraints.

In agreement with earlier investigations, our systematic study shows that the cooling instability for smooth flows – if present – manifests itself as an overstability: All quantities, e.g. the size of the cooling layer or the radiated energy, evolve in a periodic way with fixed period and amplitude. The linear stability analyses of CI and Bertschinger (1986) show that the period of the overstability of the radiative shock is determined by dimensionless quantities δ_i ($i = 0, 1, 2, \dots$) which are eigenvalues of the boundary value problem describing the flow between the radiative shock and the rear end of its cooling layer. One usually speaks of the fundamental mode (F-mode, $i = 0$) and of overtone modes (1O-mode, 2O-mode, etc). The governing eigenvalue δ is related to the steady state position of the shock, x_0 , the velocity of the inflowing matter relative to the shock, u_{in} , and the oscillation period, T , by the relation $\delta = x_0/u_{in} \cdot 2\pi/T$. Previous investigations have shown that even in the non-linear regime the period is in good agreement with the fundamental (F) and the first overtone (1O) mode determined by linear stability analysis.

However, our analysis shows – also in agreement with earlier investigations – that the overstability can show different phenomenological manifestation when oscillating in one particular mode. Therefore, we propose to introduce an additional classification of the overstability, namely the notation of types.

5.1. Different types of oscillations

Following phenomenological criteria, we propose five different oscillation types. The most striking differences between the different types are: the oscillation amplitude, which we express as $\mathcal{A} = (q_{max} - q_{min})/q_{min}$ where q is a characteristic quantity of the cooling layer, whether the oscillations are sinusoidal or not, and the oscillation mechanism. Fig. 5 and Fig. 6 illustrate the characteristics of the different types. In the following, we give only a brief description of some aspects of these types and refer to earlier authors (see Sect. 1.2) for more detailed descriptions.

The *catastrophic C-type* is characterized by a dramatic collapse of the temperature at a certain moment of the oscillation cycle. In wide ranges of the cooling layer the temperature drops nearly to nebular temperature on a very short time-scale. The density is hardly affected despite the rapid change in pressure due to the strong cooling (snapshots 4 and 5). A huge pressure cavity evolves and a secondary shock forms at the boundary to the cold layer as the pressure equilibrium starts to be re-established (visible in snapshots 3 – 6). The renewed growth sets in when the secondary shock in front of the cold layer hits the undisturbed medium again (snapshot 1). The amplitude \mathcal{A} is large and can reach up to two orders of magnitude. None

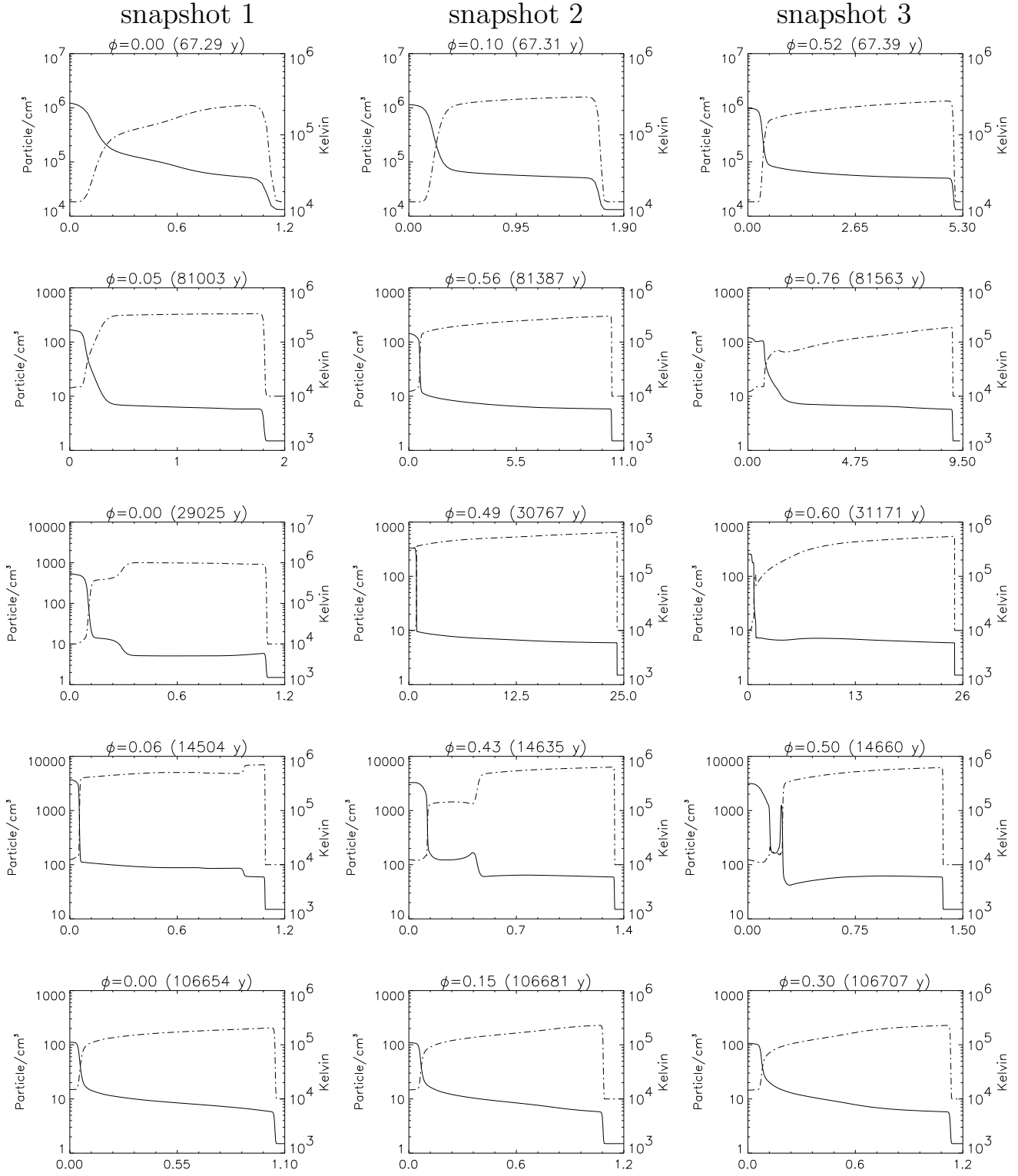


Fig. 5. a) Time-series over one oscillation cycle (from left to right) for each different type of the overstability. The series continue on the next page. Shown are the density- (solid line) and temperature-profiles (dashed line) of the cooling layer. From top to bottom: S1-type (F-mode with superimposed 1O-mode), I-type (F-mode), C-type (F-mode), M-type (1O-mode), and S2-type (1O-mode). The series correspond to the cycles shown in Fig. 6. They start approximately at the minimum extent of the shell (phase $\phi = 0$) and end at the next minimum ($\phi = 1$). (Caption continues next page.)

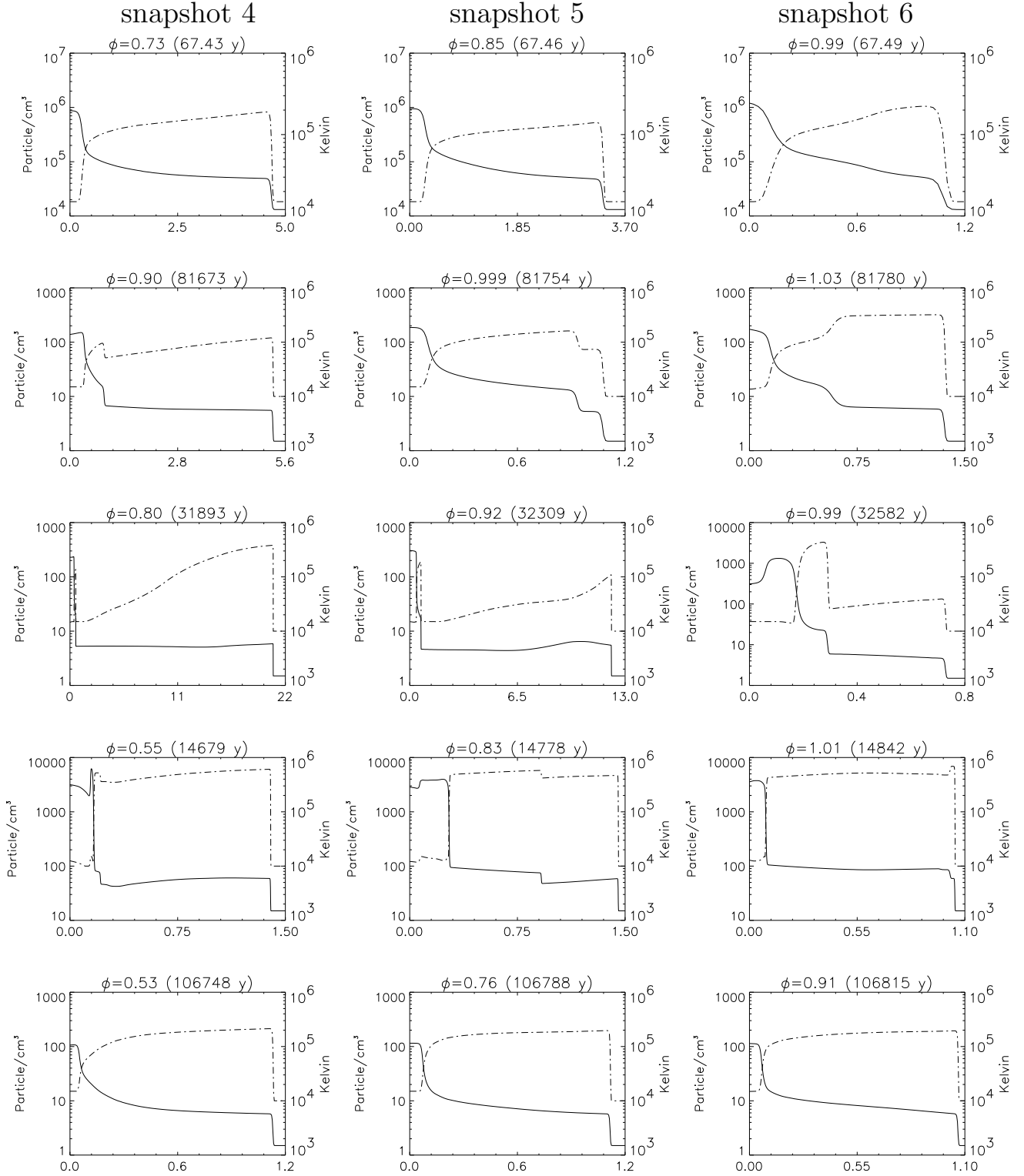


Fig. 5. b) Continuation of Fig. 5. a) of previous page. The length of the cooling layers are measured in units of the lengths of their first minima ($\phi = 0$). Notice the large difference in amplitude between the different types of oscillation for the F-mode. For the 1O-mode, the amplitude is generally small. Note that the cooling layers may have different sizes at phases $\phi = 0$ and $\phi = 1$. This is due to the influence of the dynamics in the cold dense layer (see Sect. 7) and the general deceleration of the structure. Although the types are independent of the particular flows we give in brackets the model from which we have taken the example: S1-type (CW), I-type (WB1), C-type (WB1), M-type (WB2f) and S2-type (WB1).

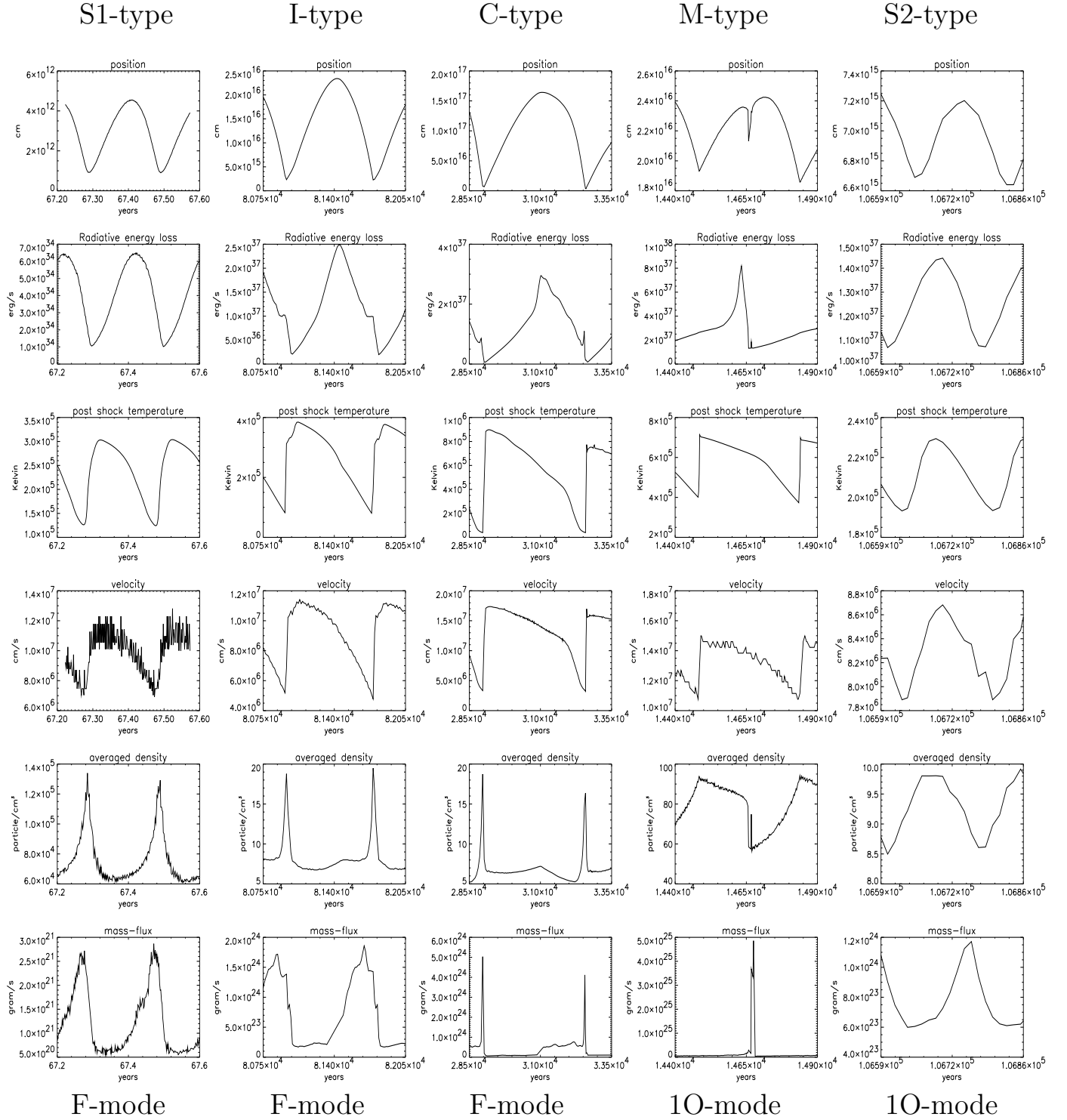


Fig. 6. The different types and modes of the cooling overstability shown in some characteristic quantities. The graphs correspond to the cycles shown in Fig. 5. From top to bottom: Size of the leading shell, radiated power (of the entire leading shell), post shock temperature, shock-velocity, average density of the leading shell and mass-flux from the leading shell into the cold compressed gas layer. Notice the highly different amplitudes of the oscillations in the different types.

of the quantities oscillates sinusoidally. In particular, the radiated energy is rather peaked. For the RLF1 we find a C-type oscillation for stationary post shock temperatures $T_{st}^{ps} > 4 \cdot 10^5$ K. The upper limit probably lies higher than $T_{st}^{ps} \approx 4 \cdot 10^6$ K, the highest limit post shock temperature we have investigated for RLF1. For the RLF2 the C-type is present between $3 \cdot 10^5$ K $< T_{st}^{ps} < 5 \cdot 10^5$ K. We observe the C-type only in the F-mode.

As another extreme, we observe the *smooth S-types*. There, the shell remains hot during the entire oscillation cycle and no pressure cavity evolves. No secondary shocks are observed. All quantities oscillate rather sinusoidally. The S1-type can be associated with the F-mode, the S2-type with the 1O-mode. \mathcal{A} is always of order one, but is generally smaller for the S2-type. In the case of the S1-type, as the shell shrinks, a pressure gradient evolves between the cold layer and the leading shock. The force it exerts leads to the renewed acceleration of the leading shock. In the case of the S2-type, on the other hand, a pressure wave evolves at the boundary to the cold layer which later hits the leading shock and accelerates it. This leads to the phase-shift between the energy loss and the size of the shell (see Fig. 6). The differences between the S1-type (F-mode) and the S2-type (1O-mode) correspond to the results of the linear analysis of CI which predict knots and phase-shifts for overtone modes. In the RLF1 we find the S2-type for temperatures $1.7 \cdot 10^5$ K $< T_{st}^{ps} < 2.5 \cdot 10^5$ K. Note that the stability limit is determined by the insufficient spatial resolution in the simulation and may be somewhat lower in reality. We find no S1-type in the RLF1. For the RLF2, we find the S1-type for temperatures between $1.8 \cdot 10^5$ K $< T_{st}^{ps} < 2.2 \cdot 10^5$ K and the S2-type for temperatures $6.6 \cdot 10^5$ K $< T_{st}^{ps} < 8.5 \cdot 10^5$ K.

The *intermediate I-type* occurs during the transition from C-type to S-types. The leading shell always remains rather hot, but – as in the C-type – the shell vanishes apart from the secondary shock. The amplitude of the oscillation is still rather big. We find the I-type for temperatures in the range of $2.5 \cdot 10^5$ K $< T_{st}^{ps} < 4 \cdot 10^5$ K for the RLF1 and in the range of $2.2 \cdot 10^5$ K $< T_{st}^{ps} < 3 \cdot 10^5$ K for the RLF2. Also the I-type is observed only in connection with the F-mode.

In the *mixed M-type* the leading shell is divided into two parts, namely a high density part near the cold layer and a low density part behind the leading shock. While the low density part remains hot the high density part strongly cools (snapshots 2 and 3). When this cooled dense matter is swallowed by the cold dense layer a pressure wave or a weak shock is generated (snapshot 4) which travels through the leading shell towards the leading shock (snapshots 4, 5 and 6). On its way it enhances the density of the areas it passes. Finally, it hits the leading shock and accelerates it (snapshot 6). By now the shell is again divided into a high density and a low density part (snapshot 6 and 1). The oscillation amplitude is of order one. Most of the energy is released during a very short time. We find

the M-type for the temperature range between $5 \cdot 10^5$ K $< T_{st}^{ps} < 6.6 \cdot 10^5$ K of the RLF2, we do not observe it for the RLF1. The M-type oscillates in the 1O-mode. Like the S2-type, the M-type shows knots and phase-shifts.

The phenomenology of the overstability and, in particular, the amplitudes of the oscillations are essentially determined by the non-linear terms. Each of the modes lives mainly in two different forms, a weak and a strong one. The *weak form* of the F-mode corresponds to the S1-type, the *strong form* to the C-type, while the *weak form* of the 1O-mode to the S2-type and the *strong form* of the 1O-mode to the M-type.

5.2. What determines the modes and the types?

We do not yet have a final answer to this question. However, we present some observations. They are mostly based on mode-transitions which occur in WB-simulations when the post-shock temperature slowly decreases due to the deceleration of the entire interaction region. We begin with two general observations.

- 1) According to our experience, for a given radiative loss function, the type of the overstability is fixed by the post-shock temperature T_{st}^{ps} of the (unstable) stationary solution alone: Different forms of excitation of the instability at the same T_{st}^{ps} result – after a certain relaxation time – in the same mode and the same type. *We detect no sign of multiple solutions or a bifurcation of the solution.*

- 2) Linear theory predicts that whenever the F-mode is present the 1O-mode is present as well. However, *in the strong forms of the F-mode we do not observe any sign of a superimposed 1O-mode*. Only at the transition from the I-type to the S-type a slight trace of a superimposed 1O-mode shows up. At this point, we observe no phase

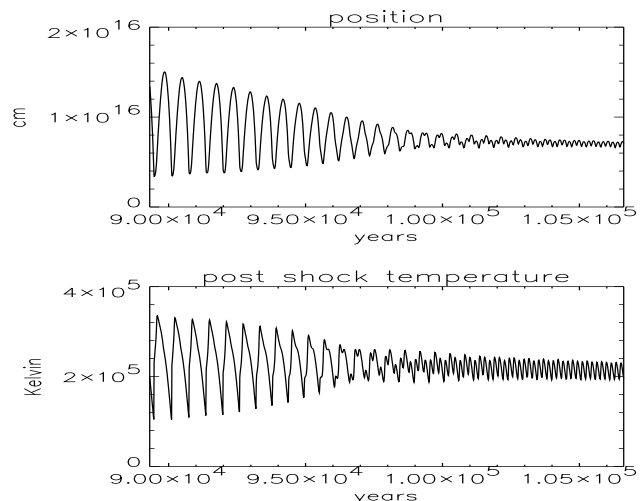


Fig. 7. Mode-transition in WB1 from the F-mode (I-type) to the 1O-mode (S2-type) for the RLF1. Shown are the time-evolution of the size of the leading shell (top) and the post-shock temperature (bottom).

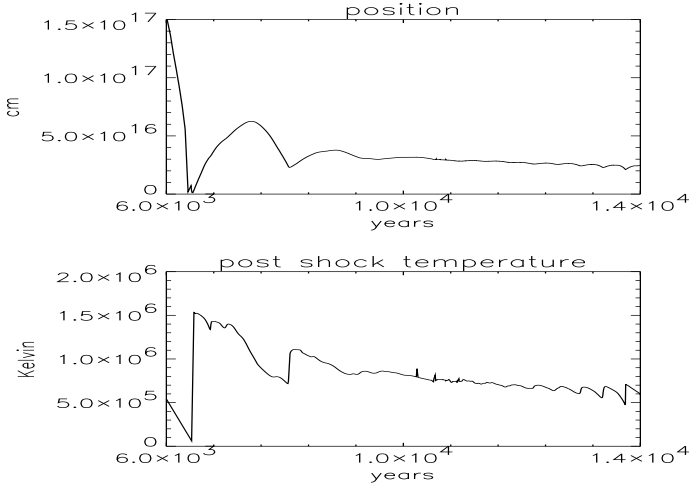


Fig. 8. WB2f: Stability behavior when applying RLF2 for $1 \cdot 10^6 > T_{st}^{ps} > 5 \cdot 10^5$. Shown is the size of the leading shell (top) and the post-shock temperature (bottom). Above $T_{st}^{ps} \approx 7 \cdot 10^5$ the (artificially excited) F-mode (C-type) is strongly damped, below this temperature a 1O-mode is growing. The further evolution is shown in the next figure.

shift between the modes due to the non-rational ratio of the eigenfrequencies. The phase shift only sets in when the overstability is already very smooth (Fig. 7). The physical reason for the absence of overtone modes in the strong forms may be the total destruction of the leading shell and, therefore, the history after each oscillation cycle.

The next two points are dealing with the transition of types and modes when scanning RLF1 in the temperature range where the logarithmic slope changes from a negative to a positive value (see Fig. 7).

- 3) We observe a mode and type-transition from the F-mode (I-type) to the 1O-mode (S2-type) at $T_{st}^{ps} \approx 2.5 \cdot 10^5$ K when applying RLF1. That is approximately the temperature where β jumps from a strongly negative value to a moderately positive value. *For this transition, the change of β associated with the post-shock temperature seems to be critical.*

- 4) The absence of the F-mode below $T_{st}^{ps} \approx 2.5 \cdot 10^5$ K for RLF1 is surprising. The post-shock temperature varies over the entire oscillation cycle between $1.9 \cdot 10^5$ K and $2.3 \cdot 10^5$ K and even most parts of the shell have always temperatures above $7.9 \cdot 10^4$ K. For these temperatures, β is equal to 0.15 while below $7.9 \cdot 10^4$ K it becomes strongly positive. Linear analysis predicts for $\beta = 0.15$ the F- and the 1O-mode to be present. Indeed, when using a RLF assuming a constant $\beta = 0.15$ we observe both modes. We conclude that *the mode is not governed by the β which is associated with the stationary post-shock temperature alone.* The entire cooling layer and, in particular, the rear boundary interface may be of similar importance. The strongly positive β for $T \leq 7.9 \cdot 10^4$ K reduces the cooling efficiency as compared to $\beta = 0.15$ and in this way seems to damp the F-mode.

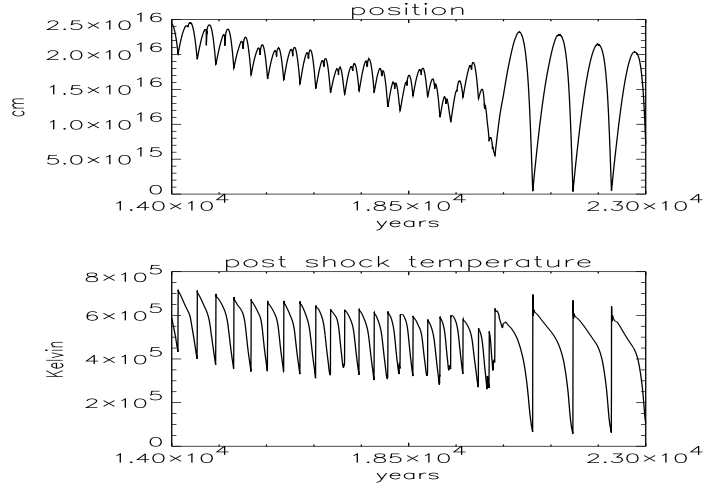


Fig. 9. WB2f: Mode-transition from 1O-mode (M-type) to F-mode (C-type) at $T_{st}^{ps} < 5 \cdot 10^5$ when applying RLF2. Shown is the size of the leading shell (top) and the post-shock temperature (bottom). (The evolution at earlier times is shown in the previous figure.)

The next three points summarize the transition of modes and types when scanning RLF2 in the temperature range $1 \cdot 10^6 \gtrsim T_{st}^{ps} \gtrsim 4 \cdot 10^5$ K (see Figs. 8 and 9). This is exactly the range where RLF2 forms a 'valley'. For $T < 4 \cdot 10^5$ K the logarithmic slope of the RLF2 is equal to -1.92, for $4 \cdot 10^5 < T < 5.37 \cdot 10^5$ K it is zero and above $5.37 \cdot 10^5$ K it is equal to 1.12. The planar models, CPF_55 to CPF_25, prove that the different modes and types observed in this 'valley region' of the RLF2 are not merely transition phenomena but persist if the structure does not slow down.

- 5) The excited F-mode (C-type) at $T_{st}^{ps} \gtrsim 9 \cdot 10^5$ K is very strongly damped when RLF2 is applied. This suggests a stable situation for this temperature, and indeed the planar model CPF_55 with $T_{st}^{ps} = 9 \cdot 10^5$ K is stable. At this temperature we have $\beta = 1.12$ which is in the stable range according to linear theory. However, large parts of the cooling layer have temperatures associated with an unstable β . Despite this fact, *in this case the β associated with the post-shock temperature seems to determine the stability.*

- 6) Below $T_{st}^{ps} \approx 8.5 \cdot 10^5$ K a 1O-mode of the S2-type grows for RLF2 (CPF_45 for $T_{st}^{ps} \approx 8.25 \cdot 10^5$ K shows S2-type behavior). The post shock temperature does not leave the region with $\beta = 1.12$ over the entire oscillation cycle. Interestingly, nearly in the entire cooling layer the temperature is in the range where $\beta = 1.12$! With decreasing T_{st}^{ps} , the type of the overstability slowly changes to the strong form of the 1O-mode (M-type) (CPF_35 for $T_{st}^{ps} \approx 6.1 \cdot 10^5$ K is clearly of the M-type). β associated with T_{st}^{ps} is still 1.12! *This again indicates that the RLF for temperatures below T_{st}^{ps} plays a significant role.*

- 7) As can be seen from Fig. 9, at $T_{st}^{ps} \approx 5 \cdot 10^5$ K another mode-transition takes place for RLF2, this time

from the IO- (M-type) to the F-mode (C-type). This temperature corresponds approximately to a change in β from the stable value 1.12 to zero, a value at which – according to linear theory – both modes should be present. *The change of β corresponding to the post-shock temperature seems to be important for the mode-transition.*

The emerging picture is not homogeneous. Sometimes, the β associated with T_{st}^{ps} seems to play an outstanding role. More often, however, the presence, the mode, and the type of the overstability cannot be determined on the basis of the local characteristics of the RLF at this temperature. We come back to these points in Sect. 8

6. The cooling instability of the leading shell for disturbed flows

6.1. The set of disturbed flows

We now discuss the cooling instability for disturbed flows. We disturb the flow upstream of the interaction zone between position r_0 and $r_0 + \lambda_0$ by setting the density to

$$\rho(r) = \rho_0 \left[1 + \xi \sin \left(\pi \frac{r - r_0}{\lambda_0} \right) \right] \text{ if } r_0 \leq r \leq r_0 + \lambda_0 \quad (11)$$

where ρ_0 is the density of the undisturbed flow. The disturbance is applied after the system has evolved into a limit cycle. The leading shock can hit it at an arbitrary phase $0 \leq \phi_0 \leq 1$ of the oscillation cycle (where $\phi = 0, 1$ are the phases of minimum extent of the leading shell). Note the difference to the setting of IGF who let the shock in its stationary position run against a, however similar, density disturbance.

We performed a systematic investigation of disturbed I-type systems on the example of WB1. All disturbances were applied around 69'000 years. The exact settings of these models can be taken from Table 5 of the appendix. Except for two models (WB1_d0 and WB1_d1) the amplitude of the disturbance, ξ , is never bigger than 1. The ratio of the mass of the disturbance, M_d , to the mean mass (over a period) of the hot leading shell, M_{ls} , varies from 0.017 to 73, the ratio of M_d to the mass of the subsequent cold dense layer, M_{cdl} , from $1.4 \cdot 10^{-4}$ to 0.6155. The ratio of the length of the disturbance, λ_0 , to the characteristic length of the limit cycle, $\ell = T \cdot v_{st}^{sh}$, varies from 0.05 to 8.8 (T denotes the oscillation period and v_{st}^{sh} the stationary shock velocity). The shock hits the disturbance at phases between $\phi_0 = 0.07$ and 0.52. The results presented in this section are a summary of the analysis of this set.

6.2. Noisy, original periodic, aperiodic, and modulated periodic evolution

We found five clearly different responses of the I-type system to disturbances. The time-evolutions of three of them are shown in Fig. 10 and a schematic representation of all possible responses is given in Fig. 11. If the disturbance is small (in which sense we see below), one ob-

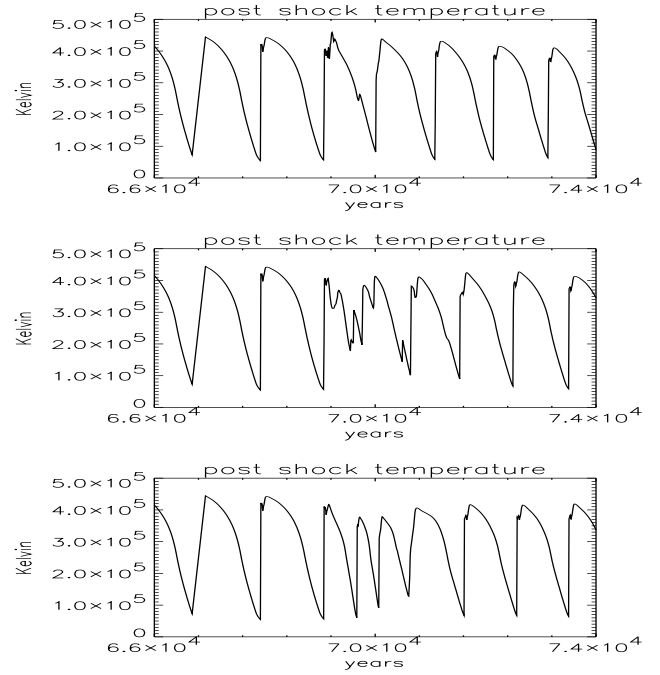


Fig. 10. Noisy original periodic, aperiodic and modulated periodic evolution of the radiative shock after being disturbed at time 68'893 years. Shown are post-shock temperatures of models WB1_d4.0.1, WB1_d4.1 and WB1_d6 (from top to bottom).

serves a rapid, aperiodic, much smaller scaled variation of only one cycle of the original oscillation. We call this a *noisy, original periodic evolution (np)*. If the disturbance is appropriately scaled, the periodicity of the limit cycle is completely destroyed and we have an *aperiodic evolution of the radiative shock (ap)*. However, after a certain time, the system relaxes to the original, periodic evolution. Disturbances on a larger length scale and not too big amplitude ξ result in a modulation of the limit cycle, governed by the slowly changing pre-shock conditions. In this case, we speak of a *modulated periodic evolution (mp)*. On the other hand, if we have a very massive disturbance

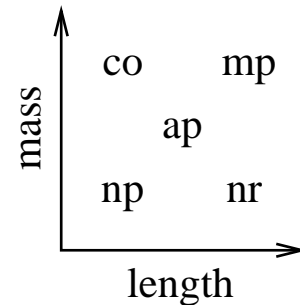


Fig. 11. Schematic representation of the different responses versus mass and length of the density disturbance.

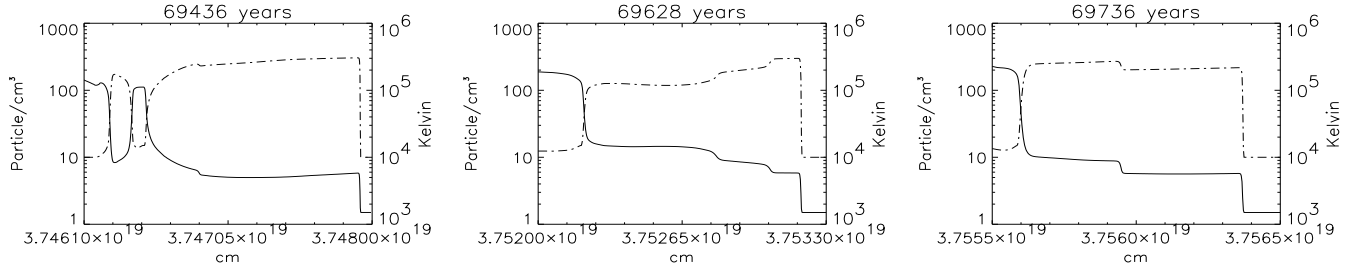


Fig. 12. The aperiodic evolution of the radiative shock and its cooling layer from example of WB1_d4.1. Shown are density- (solid line) and temperature-profiles (dashed line) of three successive times. The evolution is governed by the fast partial cooling and the waves which are created during this process. Details can be taken from Sect. 6.3.

on a relatively short length-scale, the leading *shell collapses nearly immediately (co)*. The history of the leading shell is destroyed and the shell behaves according to the new global conditions. For example, in model WB_d0 the accumulation of the mass of the disturbance by the cold dense layer leads to a slow down of the entire interaction zone and the leading shock becomes stable. Finally, if we encounter a small mass disturbance on a large length scale, the system shows nearly *no reaction (nr)*. We note already here, that big disturbances may significantly disturb the cold dense layer downstream of the radiative shock wave (see Sect. 7).

6.3. The aperiodic evolution

The oscillation mechanisms of the np- and the mp-cases are similar to the mechanisms described in Sect. 5. Here we describe the aperiodic response of the radiative shock at the example of model WB1_d4.1. It evolves very similar to what was described by IGF. We concentrate on some aspects important to the understanding of the constraints for the evolution of disturbed shocks.

The size of the initial density disturbance is crucial for the time evolution illustrated in Figs. 10 and 12. As the density disturbance passes through the leading shock it shrinks in size while being compressed. Cooling of the hot shell starts in the region with enhanced density. In fact, cooling is so fast that the flow cannot maintain pressure balance and a pressure cavity forms in the cooled region. A sheet of cold and initially over-compressed matter is then created within the hot leading shell (snapshot 1 of Fig. 12). The relaxation of the over-compressed sheet generates two pressure waves or weak shocks traveling forwards and backwards in the hot shell. Their strengths are a direct measure of the violence of formation of this second dense sheet. The dynamical consequences of these waves are twofold. Firstly, temperature and density increase again in those regions where the waves pass. The consequence for the cooling scale cannot be estimated easily, since in this region of the radiative loss function the increase in temperature and density are working in opposite directions. For RLF1 and in this temperature range the

cooling scale likely is to decrease behind weak waves, it is likely to increase behind strong waves. In our example, the first possibility applies. A second important consequence of these waves is encountered when they eventually hit the leading shock. The pushing wave transfers part of its energy to the leading shock which is accelerated. As a consequence of the shock jump conditions, the post-shock temperature is higher and the density is lower in the freshly shocked part than in the older parts of the shell (compare snapshot 2). The further development can hardly be followed in detail. The older, denser parts cool faster than the newer parts. Further cold, compressed sheets are formed, usually near the boundary to the cold layer. Their formation creates again new waves and the process continues (snapshot 3).

Our investigation proves – for the I-type range and for parameterized cooling – that this process does not last forever and that the limit cycle finally recovers.

6.4. The constraints for the evolution and relaxation times

As can be seen from Table 5 in the appendix, models having a length of the disturbance between 5 and 20 percent of the characteristic length of the limit cycle and having masses between 10 and 40 percent of the mass of the leading shell react with an aperiodic evolution to the disturbance (case ap).

To achieve the most efficient aperiodic evolution, the region of enhanced density has to be *moderately smaller* than the hot shell, since otherwise the entire leading shell would be affected nearly similarly and we would encounter a modulation of the original oscillation (case mp) or a collapse of the shell (case co). On the other hand, the region with enhanced density has to be large enough to be able to create *secondary waves* as powerful as possible, since these waves are driving the aperiodic evolution.

For the aperiodic evolution, we define the *relaxation time*, τ_{rel} , as the difference between the time when the aperiodic evolution first sets in and the time when the regular periodic evolution starts again. τ_{rel} can be taken from Table 5. The biggest ratio of τ_{rel}/τ_0 (τ_0 being the period of the limit cycle) we measured is 3 (model WB1_d4.1). In

this case, the ratio of the characteristic lengths, λ_0/ℓ_c , is 0.2, the mass ratio, M_d/M_{hls} , is 0.4. Comparing models WB1_d3, WB1_d2.2 and WB1_d4.1 we notice the influence of the different masses. A larger mass of the disturbance leads to the generation of stronger pressure waves, and the relaxation time increases.

7. The cold dense layer (CDL) and the hot leading shell (HLS): An interacting system

Downstream of the radiative shock and its cooling layer, a thin layer of cold, compressed gas is established (see Fig. 4). In this section we study the dynamics of this layer, in particular its interaction with the thermally unstable radiative shock.

7.1. Mass feeding of the CDL

We define the boundary between the cold dense layer and the hot leading shell to be at the surface where cooling is balanced by heating. Through this boundary interface, there is a net mass-flux from the cooling layer of the radiative shock into the cold dense layer which is shown in the last row of Fig. 6.

It is interesting that for smooth flows the five different types of the overstability manifest themselves also in these mass-fluxes (Fig. 6). Most remarkable, there is a very significant difference between the strong and the weak form of the overstability. For S-type instabilities the mass-fluxes are smooth and vary only moderately over one cycle. In the strong forms of the overstability, most of the mass enters the CDL during a very short time-interval of the cycle. This is a direct consequence of the sudden collapse of large amounts of the hot shell. Again we note a significant difference between the modes: In the 1O-mode (M-type), the peak of the mass-flux is correlated with the largest, in the F-mode (I- and C-types) with the smallest extension of the cooling layer. Note also that in the I- and C-type overstability the onset of the mass-flux at approximately one third of the period is accompanied by the formation of the secondary shock which is attached to the CDL. Obviously, the irregularity of the mass flux is enhanced in disturbed flows.

7.2. Response of the CDL to the cooling overstability of the leading shell

The non-steady mass-flux through the interface between the HLS and the CDL introduces disturbances into the CDL, even when smooth flows collide. Assuming that the size of the CDL is much bigger than the HLS, Bertschinger (1986) has shown by linear stability analysis that the disturbances damp on a scale which is much smaller than the size of the CDL. When we encounter the same conditions, our numerical study shows indeed this behavior. However, there are many cases where the size of the CDL and the HLS are comparable, e.g. in the period after the

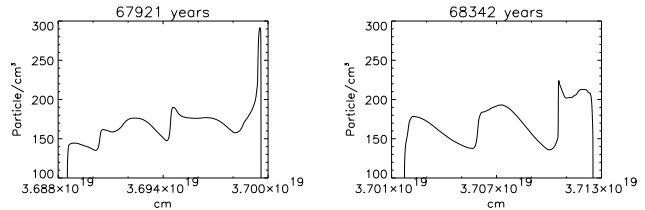


Fig. 13. Density distribution of the CDL of WB1 (I-type instability) immediately after the leading shell has collapsed and the overcompressed sheet of freshly cooled matter is swallowed by the CDL (**left**) and half a period later in the limit cycle (**right**).

transition of the shock from the adiabatic to the radiative regime. Moreover, the analysis in Sect. 7.1 shows that in strong forms of the overstability the mass feeding into the CDL – and, therefore, the introduced disturbance – is extremely pulsed with a large pulse height. When disturbed flows collide, these disturbances can become even larger. Such disturbances are clearly beyond the scope of linear analysis. Therefore, it is not surprising that under these different circumstances the disturbances can survive for a significant time.

7.2.1. Traveling waves and density variation

As described in Sect. 6.3 the sudden cooling of large parts of the hot leading shell leads to the formation of an initially overcompressed sheet of cold matter. Apparently, the same mechanism also works in the strong forms of the limit cycle of the overstability when smooth flows collide, with the difference that the newly cooled, overcompressed sheet is in contact with the already present CDL. The

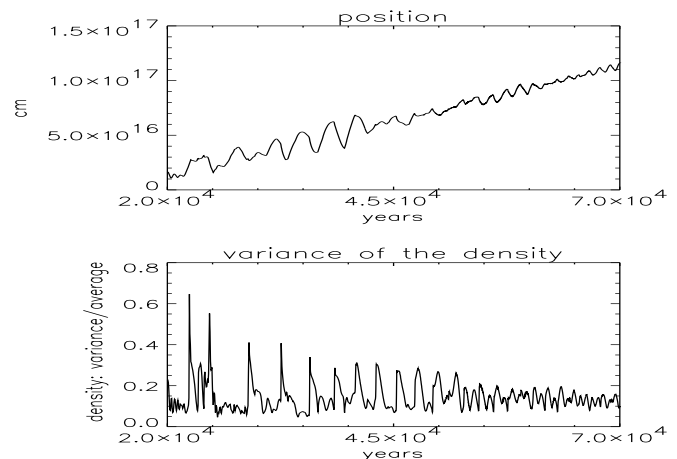


Fig. 14. Oscillating size (**top**) and density-variance σ (**bottom**) of the CDL. Shown are 18 cycles after the transition from the adiabatic to the radiative regime of model WB1. The overstability of the leading shell is of the C- and I-type.

swallowing of such an overcompressed sheet by the CDL is shown on the left of Fig. 13. The thin sheet at the very right boundary of the CDL, having approximately twice the density of the rest, contains the freshly cooled matter. At this time, the density variance in the shell is greatest (see Fig. 14). In the following, relatively quiescent phase of the limit cycle, the overcompression relaxes by a wave traveling through the CDL (right graph of Fig. 13). Eventually, the propagating wave is reflected at the rear interface of the CDL and interacts with the other waves. As a result, the density structure of the CDL is rather complicated in the presence of strong forms of the over-stability of the radiative shock. The evolution of the density variance shown in Fig. 14 exactly mirrors the cycle of the over-stability of the leading shell. It shows peaks every time a new, overcompressed sheet is incorporated into the CDL. The figure demonstrates that the density variance is rather high as long as we encounter I-type instability. Not visible in the figure, the CDL rapidly smoothes after the instability changes to S-type. Note also, that we do not find a significant difference between the density variance of an isothermal CDL (model WB1c) and an adiabatic CDL (model WB1).

7.2.2. Oscillations of the CDL

The CDL is expected to become compressed when it pushes the shock after the collapse. This should lead to a considerable shrinking of the size of the CDL, at least as long as there is not too much mass in the CDL. Indeed, we observe such oscillations (see Fig. 14). However, the traveling, reflecting, and interacting waves disturb the basic oscillation cycle remarkably. Periods of nearly no oscillation are followed by periods of nearly regular oscillation and vice-versa. When smooth flows collide, we find changes in the size of the CDL up to 15 percent as long as we encounter I-type instability in the WB and SNR simulations. Much larger oscillation of the CDL can be excited in disturbed flows as will be shown in the next paragraph.

7.3. The back-coupling to the cooling layer

We now investigate how the dynamics of the CDL affect the radiative cooling over-stability of the hot leading shell. Of course, the oscillation of the CDL changes the rear boundary conditions of the cooling layer with time, which influences the evolution of the radiative shock. This back-coupling can be strong in disturbed flows as will be demonstrated below. When smooth flows collide, the effect is present but never large (See Fig. 3). Only immediately after the transition from the adiabatic to the radiative phase it is considerable. In this phase the amplitude of the over-stable oscillation can change up to 15 percent from one period to the next. Although weaker, the effect can be observed as long as the over-stability is of the I-type.

7.3.1. The evolution of model WB1_d7

WB1_d7 is a disturbed model with a modulated periodic behavior (see Table 5). The disturbing mass is 7.3 times the average mass of the hot leading shell and 6.18 percent of the mass of the CDL. The encounter of the interaction zone with this density disturbance excites an oscillation of the CDL with an amplitude of about 15 percent. The period of the oscillation approximately corresponds to the length of the density disturbance. As demonstrated in Fig. 15, this oscillation of the CDL significantly influences the further evolution of the cooling over-stability.

Note also the direct consequence of the density disturbance for the over-stability (see again Fig. 15). The leading shock slows down. The oscillation period becomes smaller due to the decreasing cooling time. However, the radiative energy release increases due to the density enhancement which overcomes the decrease of the emitting volume due to the smaller size of the shell. When the interaction zone

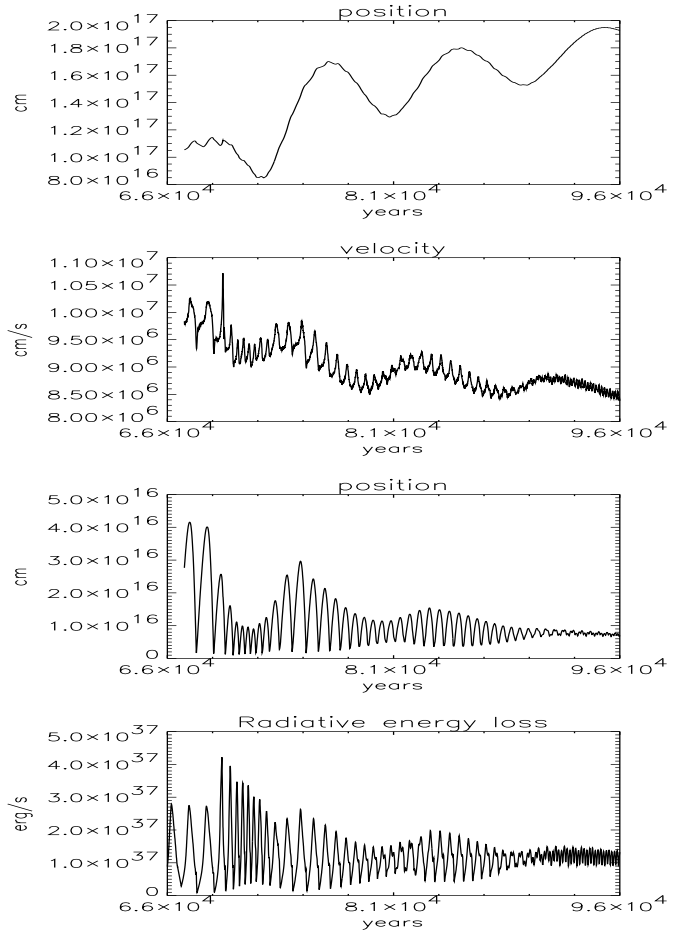


Fig. 15. Time evolution of the model WB1_d7 after running into a disturbance having 6.18 percent of the mass of the CDL. **1. line:** Size of the CDL, **2. line:** Velocity of interface between CDL and HLS, **3. line:** Size of HLS, **4. line:** Radiated energy per time from the HLS.

has passed the density peak, it accelerates again. At 73'500 years the oscillation of the leading shell has nearly recovered the state it had before the disturbance. However, the absorbed mass has led to a general slow down of the interaction zone and to the oscillation of the CDL.

7.3.2. Switch on, switch off system

The onset of the cooling instability is very sensitive to the post-shock temperature. Thus, the instability can switch on and off under the influence of an oscillatory cold dense layer as we will demonstrate with a CW calculation. At the beginning of the evolution shown in Fig. 16 a strong wave is traveling backwards and forwards in the CDL. Due to the oscillation of the CDL, the velocity of the rear boundary interface of the cooling layer is trans-critical: If the velocity falls below the critical value, the cooling instability stops, if the interface is again pushed over the critical value, the instability reappears. The overstability is of the S1-type. The instability immediately becomes periodic if the critical post-shock temperature is exceeded.

The third instable time period is most interesting. The instability is excited by a very small overshooting of the shell over the stationary value. Although the excitation is small, the amplitude of the oscillation is growing up to a value which is inherent to the system and the applied cooling function. Note that the velocity of the rear boundary

of the cooling layer is approximately constant or is even decreasing while the amplitude of the oscillation is growing. The stationary amplitude of this oscillation is nearly the same as the one in the second instable time period. The period of the limit cycle increases with time due to the decreasing density in the slow wind.

8. Discussion

8.1. What determines the types and modes?

The large sample of computations presented in this paper strongly indicates: If parameterized loss functions are applied to smooth colliding flows, a differently disturbed radiative shock wave always relaxes to the same asymptotic solution, whether this solution is stable or overstable. However, the time scale of the relaxation may strongly depend on the size and the sign of the excitation. The stationary post-shock temperature T_{st}^{ps} completely fixes the stability properties (stability limit, mode, type) of a radiative shock for a *given* RLF.

The cooling overstability in a *C-type* (*I-type*) manifests itself as runaway cooling. This requires that a significant amount of the thermal energy of the cooling layer is radiated on a time-scale which is short compared to the hydrodynamical time-scale. Thus, β has to be sufficiently negative at T_{st}^{ps} and in a sufficiently wide temperature range below. For example, this condition may be fulfilled at temperatures where line cooling of a strong coolant just sets in and abruptly enhances the cooling efficiency. *For these types, the stability properties are completely determined by the strongly negative logarithmic slope of the RLF around T_{st}^{ps} .* At least, we see hardly any difference between RLF1 and RLF2 even though the two loss functions are different for lower temperatures, except for the absolute values of the oscillation period which are due to the shift in Λ -direction by half a magnitude.

Runaway cooling and, therefore, negative β are also necessary for the occurrence of the *M-type*. Here, however, only the low temperature part at the rear end of the shell collapses. To prevent the shell from complete collapse (as in the C-type), the cooling time in the hotter front part of the shell has to be sufficiently longer than the time needed to collapse and reconstruct the rear part. This requires a sufficiently positive β at temperatures $T \approx T_{st}^{ps}$. These conditions may be fulfilled at temperatures between regions with efficient line cooling for different ions. *For this type, not only the shape of the RLF at T_{st}^{ps} is important for the stability properties, but the entire shape of the valley region.*

For the *S-types* it is necessary that the cooling time-scale at every point of the cooling layer remains of the same order as the hydrodynamical time-scale. *With the exception of the rear boundary layer, the cooling layer must have temperatures associated with moderately positive β .* For the temperatures we encounter in the rear boundary

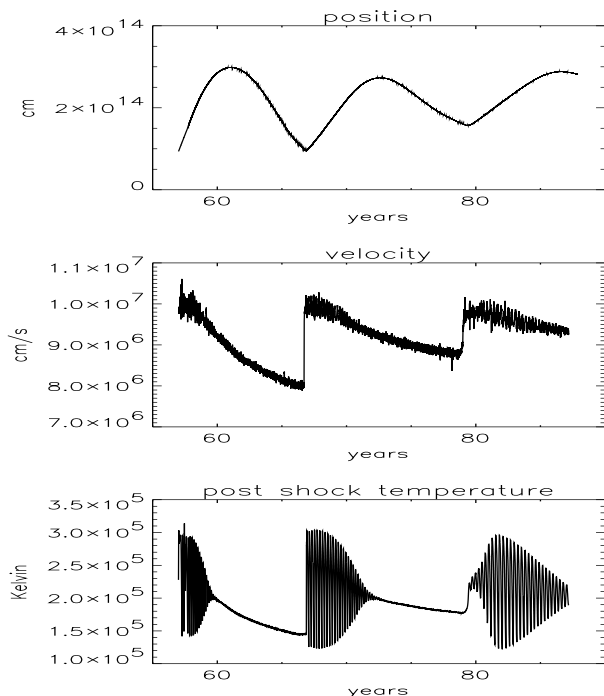


Fig. 16. The overstability switches on and off under the influence of an oscillating CDL. **Top:** Size of the CDL. **Middle:** Velocity of the interface between the CDL and the HLS. **Bottom:** Post-shock temperature of the leading shock.

layer, the shape of the RLF may be arbitrary. In particular, it can be strongly negative (e.g. for smooth types with post-shock temperatures in a valley region). This does not necessarily mean that the shape of the RLF for temperatures in the rear boundary layer is unimportant for the properties of the instability. On the contrary, we notice *the importance of the conditions in the rear boundary layer for the stability limit and the mode* in many examples.

For the modes the situation seems even more puzzling. We notice the absence of the overtone modes in the strong form of the F-mode oscillation. We ascribe this to the total destruction of information associated with each collapse of the shell. Overtone modes just have no time to grow. We emphasize the existence of a strong form of the 1O-mode which is able to radiate a substantial amount of energy. Therefore, the 1O-mode is potentially as important as the F-mode even though the temperature range of its appearance is considerably smaller. Finally, we find it remarkable that, despite the highly nonlinear character of radiative cooling, we find weak and strong forms of the overstability which, while appearing phenomenologically so differently, are governed by the same modes.

From the insight into the working mechanism of the different types one may find constraints for the transitions between them. However, there is certainly no simple way to exactly determine the stability properties at every T_{st}^{ps} .

8.2. Temperature regions with different stability properties

Based on the above discussion we propose five different stability regions for RLFs. In Fig. 17 we sketch a RLF which shows the typical behavior of most high-temperature RLFs (see e.g. Schmutzler & Tscharnuter 1993 or GEC). We note again that the boundaries between the different regions can be given only approximately, since they cannot be derived by a simple rule.

- Region I: There is always a *low-temperature stable region*, which is also present for fully time-dependent cooling. IGF and GEC found that shocks with speeds below about 130 km/s are stable.

- Region II: Here we encounter *smooth types of the overstability*. In this region, we expect the shape of the entire cooling function to be important for the stability properties. In particular, the rear boundary layer attached to the cold, compressed sheet can play a significant role. The upper boundary of this region lies at a temperature which is slightly above the point where the logarithmic slope of the RLF becomes strongly negative.

- Region III: We find strong *runaway instabilities* (C- or I-type, always F-mode) when T_{st}^{ps} lies in a region of the RLF with negative logarithmic slope **and** T_{st}^{ps} is sufficiently above the low-temperature edge of the negative slope region. Under these conditions, the overstability is nearly independent of the shape of the RLF at lower temperatures.

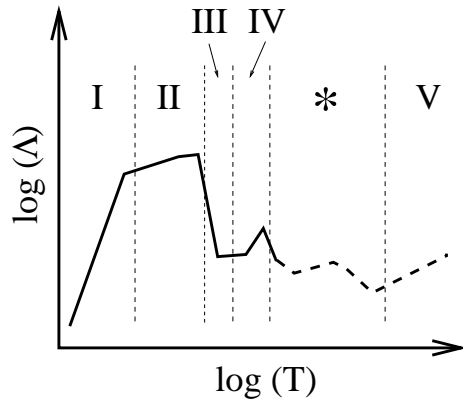


Fig. 17. Sketch of a typical radiative loss function $\Lambda(T)$ on a log-log scale. The solid line denotes the region we have extensively investigated, the dashed line denotes the high-temperature region we have not investigated. Shown are the five qualitatively different stability regions. region I: stable; region II: smooth types; region III: runaway cooling; region IV: valley region; region *: behavior not known; region V: Bremsstrahlung region.

- Region IV: This region is associated with a *valley in the RLF* which determines the stability properties. Note, that the valley is larger than stability region IV (e.g. between $1.6 \cdot 10^5$ and $1 \cdot 10^6$ K in RLF2). The shape of the RLF below the valley seems of minor importance. The strong form of the 1O-mode (M-type) can only occur in such a region. In addition, we find in this region the strong form of the F-mode as well as the smooth form of the 1O-mode and even stable behavior. For this region it seems hardly possible to predict whether or not, and in which mode and type, the overstability is present. Any real shock which is slightly disturbed can abruptly change into any of these types. In this sense, the shock reacts truly chaotic in this region.

- Region V: *High-temperature Bremsstrahlung region* with $\beta = 0.5$. Although we have not done any experiment in this region we predict a smooth S2-type oscillation if we are sufficiently far away from the low-temperature boundary where the logarithmic slope flattens to $\beta \lesssim 0.5$. Near the low-temperature boundary the existence of a F-mode may be possible. Also in this region the rear boundary layer of the hot shell may be important for the stability property.

8.3. Parameterized radiative loss function versus more elaborated models

IGF and GEC emphasize the need for fully time-dependent radiation hydrodynamical calculations which explicitly include ionization, recombination and non-equilibrium line-cooling, and we completely agree with them. However, such computations are very costly. At present and even in the near future, systematic longtime

Radiative cooling overstability in colliding flows							
types		characteristics					
F-mode	1O-mode	strength	oscillation amplitude F-mode	$\tau_{\text{cool}} / \tau_{\text{hydro}}$	collapsing shell	cools temp. to nebular T	secondary shocks
S1-type	S2-type	weak	order one	≈ 1 always	no	no	none
I-type		moderate	one magnitude	temp. $\lesssim 1$	slow collapse	no	weak
C-type	M-type	strong	up to two magnitudes	temp. $\ll 1$	yes	yes	strong

Table 1. Schematic summary of the classification and the characteristics for the spherically symmetric cooling overstability. T stands for temperature and temp. for temporarily. Note, the oscillation amplitude of the 1O-mode is always of order one, also for the strong form.

evolution and multi-dimensional computations cannot be done using such an approach. One has, therefore, to deal with the use of parameterized loss functions. Some of the major short comings of parameterized RLFs compared to fully time dependent computations have already been mentioned in Sect 2.2, and were discussed in some more detail by GEC and IGF. A key point is that the ionization structure of the plasma does not necessarily correspond to the gas temperature. The cooling history is often crucial for the determination of the ionization structure. Consequently, the correct cooling rate cannot be described by a function of the temperature alone as in the case of a RLF.

In the runaway cooling range ($u_{in} \approx 200$ km/s), GEC directly compare one example of the fully time-dependent model with simulations applying two differently parameterized models (their Fig. 3). The global dynamics resulting from the two different approaches qualitatively coincide. The oscillation period and amplitude differ by some percent. *For the runaway cooling range* this result is not surprising. However, in cooling regions II and IV we assume that the correct shock dynamics is less well mirrored when using a RLF. Here, the stability properties cannot be pinned down to the shape of the loss function around T_{st}^{ps} . A time dependent computation in this regime may yield different overall dynamics.

Generally, newly shocked matter is likely to be underionized, whereas gas on its cooling track tends to be overionized. *In regions II and III underionization tends to stabilize the shock* since the effective cooling function flattens compared to the parameterized function at this temperature (see Fig. 2 of GEC). The influence of a possible overionization at lower temperature will not change this picture, because lower temperatures are of minor importance for runaway cooling. On the other hand, *in the valley stability region IV, underionization tends to decrease the logarithmic slope of the effective loss function at T_{st}^{ps} , and has probably a destabilizing effect.* Overionization along the cooling track may slightly reduce the size of the collapsing part at the rear end of the cooling layer.

Partly based on the global similarity between fully time dependent computations and RLF computations GEC suggested that the overall stability properties of a

radiative shock can be determined by the local β at the high temperature end of the recombination zone, at least if only small perturbations of the steady state shock are considered. As has been demonstrated in this paper, this local condition applies only in runaway cooling regions. For other stability types we assume that the importance of the cooling behavior at lower temperatures persists also in a time-dependent computation.

Also GEC have shown that *some important details are missed or are different in the parameterized model*, even in cases where the overall dynamics are relatively well captured by parameterized cooling. In addition, IGF have found *considerable differences between calculated spectra for equilibrium and non-equilibrium cooling shocks*. In general, we feel that the question of how well the use of parameterized radiative loss functions can replace fully time-dependent calculations badly needs further investigation. Not only as far as the global dynamics are concerned but also with regard to diagnostics. A future perspective may be the use of improved parameterized models, e.g. the use of several different radiative loss functions, to better account for the different cooling histories

9. Conclusion

Before drawing conclusions from this systematic study of the long-term evolution of the radiative cooling instability in colliding flows we emphasize that these results hold for parameterized cooling of the form $N^2 \cdot \Lambda(T)$. Possible relevances for fully time-dependent cooling are discussed in Sect. 8. Even though most of the results are obtained by computing spherically symmetric flows, the conclusions are only reliable for planar flows, since the size of the radiative shock is much smaller than the radius of the structure.

We emphasize the many *different manifestations of the cooling overstability*. For both practically important modes, the fundamental and first overtone mode, we find a strong and a weak form of the overstability. The key point for the distinction between these two forms is the ratio of the two governing time scales, $\eta = \tau_{\text{cool}}/\tau_{\text{hydro}}$, which in the strong forms may be temporarily very small but

which is always of order one in the weak forms. We, therefore, propose the introduction of different phenomenological types as summarized in Table 1.

The system always relaxes to the *same asymptotic oscillatory or stable solution* which only depends on the stationary post-shock temperature. This asymptotic solution is independent of the sign and the size of the disturbance. It is possible to distinguish five qualitatively different stability regions with different stability properties. Even though the importance of the different shapes of the RLF in different temperature regions can be roughly estimated, we find no easy criterion which determines the stability properties, neither the stability limit, nor the mode, nor the type. In particular, we find many examples in which the logarithmic slope of the RLF at the stationary post-shock temperature is not the only relevant parameter for the stability behavior.

Probably *not all radiative shocks are unstable above a certain threshold velocity* of the stationary shock. Due to the existence of 'valleys' in the radiative loss function we find stable islands or smooth types of the instability even for high velocities. A necessary but not sufficient condition for their occurrence is a logarithmic slope of the radiative loss function which according to linear theory is stable at the stationary post-shock temperature. We also find a strong form of the first overtone mode, which exists in such valley regions.

We find different *evolutionary scenarios when radiative shocks run into a single density disturbance*. The system reacts aperiodic only if the length and the mass of the disturbance are appropriately scaled. If they are too small we find only a moderate, short reaction but the system remains in the original limit cycle. If the length is too big the system has time to adjust itself and the oscillations are modulated according to the new pre-shock conditions. If the mass is too large, the shell collapses immediately and its history is destroyed.

The *cold compressed gas* downstream of an interstellar radiative shock can be important for the stability of the shock. When smooth flows collide, this layer is to a minor degree (ten percent effects) dynamically important in the strong forms of the instability. However, a density disturbance in the flow on the order of a few percent of the mass of the layer leads to a significant dynamical influence of the layer. As long as we encounter strong forms of the overstability, the cold dense layer shows a rich internal structure.

The *numerical method* and the *coarseness of the numerical grid* can significantly influence the computed solutions. The entire instability or any particular mode can vanish only due to a too coarse mesh combined with an inappropriate numerical method. This effect is most probably present in all multidimensional calculations.

A. Appendix

number	range	β	$3k_B/2\Lambda_0$	$\tau \cdot N$
1	0.70 – 1.35 (4)	4.64	4.6 (25)	4.2 (10)
2	1.35 – 2.00 (4)	2.43	3.4 (16)	2.5 (10)
3	2.00 – 2.69 (4)	-0.30	6.3 (4)	3.7 (10)
4	2.69 – 7.94 (4)	1.48	4.8 (12)	2.2 (10)
5	0.79 – 2.63 (5)	0.15	1.5 (6)	6.0 (10)
6	2.63 – 4.17 (5)	-2.23	1.9 (-7)	2.7 (11)
7	4.17 – 5.62 (5)	0.16	5.4 (6)	3.5 (11)
8	0.56 – 2.00 (6)	-0.56	4.0 (2)	9.7 (11)
9	2.00 – 3.31 (6)	-2.27	1.9 (-8)	3.8 (13)
10	0.33 – 10.0 (7)	0.00	1.2 (7)	1.2 (15)
11	0.10 – 5.00 (9)	0.50	1.2 (11)	8.2 (15)

Table 2. RLF1 based on the loss function by Cook et al. (1989).

number	range	β	$3k_B/2\Lambda_0$	$\tau \cdot N$
1	0.79 – 1.82 (4)	4.06	7.2 (23)	6.9 (10)
2	1.82 – 2.51 (4)	1.71	7.6 (13)	5.5 (10)
3	2.51 – 3.80 (4)	0.56	6.1 (8)	6.5 (10)
4	0.38 – 1.58 (5)	0.79	7.1 (9)	8.8 (10)
5	1.58 – 2.19 (5)	-0.50	1.4 (3)	1.4 (11)
6	2.19 – 3.98 (5)	-1.92	3.5 (-5)	8.2 (11)
7	3.98 – 5.37 (5)	0.00	2.1 (6)	1.1 (12)
8	5.37 – 9.55 (5)	1.12	5.4 (12)	1.0 (12)
9	0.95 – 1.41 (6)	-0.82	1.3 (1)	2.1 (12)
10	1.41 – 2.40 (6)	-2.35	5.4 (-9)	1.2 (13)
11	2.40 – 3.98 (6)	-0.77	6.1 (1)	3.1 (13)
12	3.98 – 8.91 (6)	-0.09	2.1 (6)	7.3 (13)
13	0.89 – 1.74 (7)	-0.45	2.0 (10)	2.0 (14)
14	1.74 – 3.02 (7)	0.13	8.9 (7)	3.1 (14)
15	0.30 – 1.00 (8)	0.39	7.9 (9)	6.5 (14)
16	0.10 – 5.00 (9)	0.50	6.5 (10)	4.6 (15)

Table 3. RLF2 based on the time-dependent loss function by Schmutzler and Tscharnuter (1993).

Acknowledgements. We thank the crew of ETH running the Cray supercomputer for steady support, Harry Nussbaumer for his comments on the manuscript, and the referee, Roger Chevalier, for useful comments which improved the manuscript. R.W. was supported by the ETH Forschungskredit, D.F. by the Schweizerischer Nationalfond.

References

- Berger M. J., 1985, Lectures in applied Mathematics 22, 31
- Berger M. J., LeVeque R. J., 1989, in AIAA 9th Computational Fluid Dynamics Conference, Buffalo, NY, No. 89-1930-CP in AIAA-Papers

Model	Wind bubble (WB)										
	geometry			characteristics		wind of central star			interstellar medium		
	r_{\min}	r_{\max}	Δr	RLF	T_C/T_H	massloss	vel.	temp.	N	vel.	temp.
	cm	cm	cm		$^{\circ}\text{K}$	M_{\odot}/y	km/s	$^{\circ}\text{K}$	cm^3	km/s	$^{\circ}\text{K}$
WB1	1.6 (17)	1 (20)	2.4 (13)	1	15/10	1 (-4)	1.6 (3)	15	1.5	0	10
WB1e	1.6 (17)	1 (20)	2.4 (13)	1	10/10	1 (-4)	1.6 (3)	15	1.5	0	10
WB2	1.6 (17)	1 (20)	2.4 (13)	2	15/10	1 (-4)	1.6 (3)	15	1.5	0	10
WB1f	1.6 (17)	1 (19)	3.0 (11)	1	15/10	1 (-4)	3.0 (3)	15	75	0	10
WB2f	1.6 (17)	1 (20)	2.4 (13)	2	15/10	1 (-4)	2.8 (3)	15	15	0	10
	Supernova remnant (SNR)										
	geometry			characteristics		stellar blast			interstellar medium		
	r_{\min}	r_{\max}	Δr	RLF	T_C/T_H	mass	energy	temp.	N	vel.	temp.
	cm	cm	cm		$^{\circ}\text{K}$	M_{\odot}	ergs	$^{\circ}\text{K}$	cm^3	km/s	$^{\circ}\text{K}$
SNR1	1 (16)	1 (21)	4.9 (14)	1	15/10	50	1 (51)	15	1	0	10
SNR2	1 (16)	1 (21)	6.1 (13)	2	15/10	50	1 (51)	15	1	0	10
	Colliding winds (CW)										
	geometry			characteristics		present wind of CS			earlier wind of CS		
	r_{\min}	r_{\max}	Δr	RLF	T_C/T_H	massloss	vel.	temp.	massloss	vel.	temp.
	cm	cm	cm		$^{\circ}\text{K}$	M_{\odot}/y	km/s	$^{\circ}\text{K}$	M_{\odot}/y	km/s	$^{\circ}\text{K}$
CW	5 (15)	1 (17)	2.3 (10)	2	15/15	1.1 (-7)	2.5 (3)	15	2 (-6)	20	15
	Colliding planar flows (CPF)										
	Instability	geometry		characteristics		driving wind			interstellar medium		
	type	domain	Δr	RLF	T_C/T_H	density	vel.	temp.	density	vel.	temp.
		cm	cm		$^{\circ}\text{K}$	cm^{-3}	km/s	$^{\circ}\text{K}$	cm^{-3}	km/s	$^{\circ}\text{K}$
CPF_25	C	1 (20)	2.4(13)	2	15/10	0.025	2800	15	15	0	10
CPF_35	M	1 (20)	2.4(13)	2	15/10	0.035	2800	15	15	0	10
CPF_45	S2	1 (20)	2.4(13)	2	15/10	0.045	2800	15	15	0	10
CPF_55	stable	1 (20)	2.4(13)	2	15/10	0.055	2800	15	15	0	10

Table 4. Sample of computed colliding smooth flows. As a representative for the *wind bubble* flow we take NGC 6880 (WR 136). We assume model parameters as derived by Schmutz et al. (1989). In addition, we compute models with faster winds (models .f). For the *supernova remnant* we assume the same parameters as Bertschinger (1986). 80 percent of the initial energy is thermal in our models. For the *colliding wind* we take the same parameters as Icke et al. (1992) took for their (2D) model of an (aspherical) planetary nebulae for the *colliding wind* model. r_{\min} and r_{\max} denote the minimum and maximum extent of the computational domain. Δr denotes the finest spatial discretization of the computational mesh. T_C denotes the cooling limit, T_H the heating limit. CS stands for central star.

- Bertschinger E., 1986, ApJ 304, 154
Chevalier R. A., Imamura J. N., 1982, ApJ 261, 543, (CI)
Chevalier R. A., Imamura J. N., 1983, ApJ 270, 554
Colella P., Glaz H. M., 1984, Journal of Computational Physics 59, 264
Colella P., Majda A., Roytburd V., 1986, SIAM J.Sci. Stat. Comput. 4, 1059
Cook J. W., Cheng C.-C., Jacobs V. L., Antiochos S. K., 1989, ApJ 338, 1176
Dgani R., Soker N., Cadavid M. L., 1995, AJ 110(4), 1894
Falle S. A. E. G., 1975, MNRAS 172, 55
Falle S. A. E. G., 1981, MNRAS 195, 1011
Gaetz T. J., Edgar J., Chevalier R. A., 1988, ApJ 329, 927, (GEC)
Houck J. C., Chevalier R. A., 1992, ApJ 395, 592
Icke V., Balick B., Frank A., 1992, A&A 253, 224
Imamura J. N., Wolff M. T., 1990, ApJ 355, 216
Imamura J. N., Wolff M. T., Durisen R. H., 1984, ApJ 276, 667
Innes D. E., 1988, in W. Kundt (ed.), Supernova Shells and Their Birth Events, Vol. 316 of *Lecture Notes in Physics*, p. 74
Innes D. E., Giddings J. R., Falle S. A. E. G., 1987, MNRAS 226, 67, (IGF)
Klingenstein P., 1994, Hyperbolic Conservation Laws: Errors of the shock location, Technical Report 94-07, Seminar für Angewandte Mathematik, Eidgenössische Technische Hochschule, Zürich, Switzerland
Langer S. H., Chanmugam G., Shaviv G., 1981, ApJ 245, L23
Langer S. H., Chanmugam G., Shaviv G., 1982, ApJ 258, 289
LeVeque R., Yee H., 1990, Journal of Computational Physics 86, 187

number	model WB1	ξ	λ_0 10^{17} cm	λ_0/ℓ_c	M_d 10^{33} gr	M_d/M_{hls}	M_d/M_{cdl}	ϕ_0	response	τ_{rel}/τ_0
0	_d0	64	30	8.8	7000	1170	10	0.17	co	
1	_d2.1	0.75	0.67	0.2	1.83	0.305	0.0026	0.07	ap	2.4
2	_d2.2	0.75	0.67	0.2	1.83	0.305	0.0026	0.14	ap	2.4
3	_d2.3	0.75	0.67	0.2	1.83	0.305	0.0026	0.52	ap	2.5
4	_d3	0.5	0.67	0.2	1.22	0.203	0.0017	0.14	ap	1.6
2	_d2.2	0.75	0.67	0.2	1.83	0.305	0.0026	0.14	ap	2.4
5	_d4.1	1	0.67	0.2	2.44	0.407	0.0034	0.14	ap	3.0
6	_d4.0.2	0.5	0.028	0.0083	0.10	0.017	0.00014	0.14	nop	
4	_d3	0.5	0.67	0.2	1.22	0.203	0.0017	0.14	ap	1.6
14	_d5	0.5	4.34	1.28	7.91	1.318	0.0111	0.14	mp	
7	_d4.0.1	1	0.0566	0.0166	0.20	0.033	0.00028	0.14	nop	
8	_d4.0.0	1	0.17	0.05	0.61	0.102	0.00086	0.14	ap	1.6
9	_d4.0	1	0.33	0.1	1.22	0.203	0.0017	0.14	ap	1.7
5	_d4.1	1	0.67	0.2	2.44	0.407	0.0034	0.14	ap	3.0
10	_d4	1	1.34	0.4	4.88	0.813	0.0069	0.14	mp	
11	_d6	1	4.02	1.18	14.6	2.433	0.0206	0.14	mp	
12	_d7	1	12.06	3.55	43.9	7.317	0.0618	0.14	mp	
13	_d1	4.14	30.00	8.8	437	73	0.6155	0.17	mp	
14	_d5	0.5	4.34	1.28	7.91	1.318	0.0111	0.14	mp	

Table 5. Sample of the disturbed flows discussed in Sect. 6. We disturb model WB1 (see Table 4) according to Eq. 13 at a time of approximately 69'000 years where we encounter typical I-type overstability. The period of the limit cycle, τ_0 , is approximately 1100 years. The mean mass M_{ls} of the leading shell is approximately $6 \cdot 10^{33}$ gram. The rear boundary of the leading shell has a mean velocity of $9.95 \cdot 10^6$ cm/s. Multiplication with the period of the limit cycle yields a characteristic length $\ell_c \approx 3.4 \cdot 10^{17}$ cm. The mass M_{cdl} of the cold dense layer is $7.1 \cdot 10^{35}$ gram. M_d denotes the mass, λ_0 the length and ξ the amplitude of the disturbance. ϕ_0 denotes the phase of the limit cycle at which the leading shock hits the disturbance. τ_{rel} denotes the relaxation time for the aperiodic cases (*ap*). The other cases are: *nop*: noisy original periodic evolution, *mp*: modulated periodic evolution, (*co*:) collapse of the leading shell. Note that some models may be listed several times to better illustrate dependences.

Plewa T., 1995, MNRAS 275, 143
Ryu D., Vishniac E. T., 1991, ApJ 368, 411
Schmutz W., Hamann W.-R., Wessolowski U., 1989, A&A
210, 236
Schmutzler T., Tscharnuter W. M., 1993, A&A 273, 318
Strickland R., Blondin J. M., 1995, ApJ 449, 727
Walder R., 1993, *Ph.D. thesis*, ETH Zürich
Wolff M. T., Gardner J. H., Wood K. S., 1989, ApJ 346,
833